The Uranus Multi-Experiment Radiometer for Haze and Clouds Characterization

V. Apéstigue[1] · D. Toledo[1] · P.G.J. Irwin[2] · P. Rannou[3] · A. Gonzalo[1] ·
J. Martínez-Oter[1] · J. Ceballos-Cáceres[4] · J. Azcue[1] · J.J. Jiménez[1] · E. Sebastian[1,5] ·
M. Yela[1] · M. Sorribas[1] · J.R. de Mingo[1] · A. Martín-Ortega[1] · T. Belenger[1] · M. Alvarez[1] ·
D. Vázquez-García de la Vega[4] · S. Espejo[4] · I. Arruego[1]

Abstract

The aerosols (clouds and hazes) on Uranus are one of the main elements for understanding the thermal structure and dynamics of its atmosphere. Aerosol particles absorb and scatter the solar radiation, directly affecting the energy balance that drives the atmospheric dynamics of the planet. In this sense, aerosol information such as the vertical distribution or optical properties is essential for characterizing the interactions between sunlight and aerosol particles at each altitude in the atmosphere and for understanding the energy balance of the planet's atmosphere. Moreover, the distribution of aerosols in the atmosphere provides key information on the global circulation of the planet (e.g., regions of upwelling or subsidence).

To address this challenge, we propose the Uranus Multi-experiment Radiometer (UMR), a lightweight instrument designed to characterize the aerosols in Uranus' atmosphere as part of the upcoming Uranus Flagship mission's descending probe payload. The scientific goals of UMR are: (1) to study the variation of the solar radiation in the ultra-violet (UV) with altitude and characterize the energy deposition in the atmosphere; (2) to study the vertical distribution of the hazes and clouds and characterize their scattering and optical properties; (3) to investigate the heating rates of the atmosphere by directly measuring the upward and downward fluxes; and (4) to study the cloud vertical distribution and composition at pressures where sunlight is practically negligible (p > 4-5 bars).

The instrument includes a set of photodetectors, field-of-view masks, a light infrared lamp, and interference filters. It draws on the heritage of previous instruments developed at the Instituto Nacional de Técnica Aeroespacial (INTA) that participated in the exploration of Mars, where similar technology has demonstrated its endurance in extreme environments while utilizing limited resources regarding power consumption, mass and volume footprints, and data budget. The radiometer's design and characteristics make it a valuable complementary payload for studying Uranus' atmosphere with a high scientific return.

Keywords Planetary radiometer · Ice Giants · Uranus · Clouds and haze

1 Introduction

Uranus and Neptune, known as the Ice Giants, stand out as the only planets in the Solar System that have not been the focus of dedicated missions. However, delving into the study

---

Extended author information available on the last page of the article

of these planets is essential for us to grasp how our planetary system formed (Mandt et al. 2015) and changed over time (Mousis et al. 2022), especially since ice planet systems are quite common in other planetary systems (Borucki et al. 2011; Fulton et al. 2017).

Our current understanding mainly comes from "limited" observations made by Earth and space telescopes and a brief visit by the Voyager 2 spacecraft over thirty years ago. According to the recent Decadal Survey Report (National Academies 2022), NASA has placed a priority on sending a significant mission to Uranus, in addition to their ongoing missions to Mars and Europa. Similarly, the Voyage 2050 study (ESA Senior Committee, 2021) by the European Space Agency (ESA) aligns with this direction, suggesting that ESA should join forces in a future mission through collaboration, following the successful model of partnerships in Cassini-Huygens.

During the last two decades, several reference missions have been proposed to reach the Ice Giants system (Hubbard et al. 2010; Arridge et al. 2012; Hofstadter et al. 2017, 2019; Bayon et al. 2019). These mission proposals aim to investigate the optimal arrangement for accomplishing a number of scientific goals using the available technology at the time. The most recent and comprehensive study conducted to achieve the scientific objectives of the last Decadal report is the Uranus Orbiter and Probe (UOP) mission (Simon et al. 2021). This Flagship-class mission concept consists of an orbiter and a descent probe to be launched preferably by 2031.

For the orbiter, the scientific priorities extracted from the Decadal Survey are: to study the planet's bulk composition and internal structure, the magnetic field, the atmosphere circulation, the rings, and the satellite system. To this end, the spacecraft includes as referenced payload package of six instruments. In the case of the descent probe, its primary mission is to obtain the atmospheric noble gas abundances, noble gas isotope ratios, and the thermal structure of the atmosphere and winds, using four reference instruments: an Atmospheric Structure Instrument, a Mass Spectrometer, an Ultra Stable Oscillator, and an Ortho-Para Hydrogen Sensor.

However, these probes could also be capable of studying the hazes composed of small photochemically produced particles (hydrocarbon ices) and the abundances of species that can condense in the atmosphere and form clouds, such as NH_3, CH_4, H_2S, and H_2O. These aerosol particles are crucial in the radiative heat budget of the planet, and measuring their optical properties and spatial distribution can provide useful information about the chemistry and dynamics of the Uranus stratosphere and troposphere, constraining planetary formation models (e.g., Atreya et al. 2020; Mousis et al. 2018). Orbital observations could give partial information about these atmospheric structured layers but to give a "ground truth" of the vertical distribution and composition of the aerosols we need the use of a descent probe with dedicated instrumentation and in-situ observations compatible with the resources of the probe's primary mission.

2 Descent Probes Aerosol Instrumentation Precedents

Historically, descent probes have incorporated instrumentation for the study of clouds based on the optical properties of their aerosols, and the deposition of solar energy as a function of altitude. The Russian Venera program, in its descent probe of mission number 8, employed a visible-light photometer. Its purpose was to obtain the optimal exposure value for future surface photographs of Venus, which would be sought in the subsequent missions. However, this instrument also conducted the initial measurements of solar radiation variation in Venus' atmosphere (Avduevsky et al. 1973) during the descent. The Venera 9,

10, and 11 descent probes included nephelometers (back and multi-scattering angles). They helped identify three cloud layers and the underlying haze. As a result, they could determine the microphysical properties of the particles in these layers (Marov et al. 1980). In 1978, the Pioneer mission, also dedicated to the study of Venus, deployed a set of atmospheric probes alongside an orbiter. The Venus Sounder Probe was the largest and most complete descent module, equipped with 11 instruments, out of which 4 were focused on the analysis of aerosols and thermal balance a backscattering nephelometer (Ragent et al. 1980), a solar flux radiometer (Tomasko et al. 1980), an infrared radiometer (Boese et al. 1980), and a cloud particle size spectrometer (Knollenberg and Gilland 1980). On the other hand, the other three smaller twin probes were outfitted with 7 instruments, of which 2 were also dedicated to cloud studies: the same nephelometer as in the main probe (Ragent et al. 1980) and a miniaturized net flux radiometer (Sromovsky et al. 1980).

In 1995, the Galileo probe conducted the first in-situ exploration of the atmosphere of a giant planet. During its descent of over 150 km, it studied Jupiter's aerosols using a nephelometer (Ragent et al. 1992) capable of measuring simultaneously the scattering properties of particles at 5 different angles, drawing inspiration from the Venera nephelometers. Additionally, the probe included Galileo's Net Flux Radiometer (Sromovsky et al. 1992) for the atmosphere energy balance determination.

Finally, there is the precedent of the Huygens probe for the Cassini mission, developed jointly by NASA and ESA, with the objective of studying the atmosphere of Titan. In this case, the Descent Imager/Spectral Radiometer (DISR) was the key instrument for the characterization of the aerosols (Tomasko et al. 2002). It encompassed the measurement of total solar radiation flux as well as measurements of scattering in two spectral bands and across two polarization planes, along with wavelength-dependent extinction measurements across different layers of the atmosphere. Moreover, it incorporated a camera system to capture winds and details of the Titan's surface.

Although the spatial coverage of the probe observations is very limited compared with the orbital observations, the characterization of the atmosphere (e.g., the aerosols) with in-situ measurements is carried out with a level of detail that is not achievable from orbiter observations. Consequently, various instruments have been proposed in recent years for the descent probe of a prospective Ice Giant Mission. One such instrument is the Nef Flux Radiometer (Aslam et al. 2020), which builds upon the legacy of the aforementioned NFR instrument from Galileo's mission. Its objective is to measure the atmospheric heat balance and structure, the three-dimensional flow in the troposphere, and the compositions and opacities of the cloud layers. Another notable instrument is the LONSCAPE nephelometer and particle counter (Renard et al. 2020). This instrument was proposed to retrieve both the concentrations and phase functions of aerosols in the range of 0.2 to 50 μm, thereby constraining their composition and formation process.

3 Instrument Concept

The characterization of aerosols in the various planetary atmospheres visited by descent probe missions has been crucial for comprehending their global atmospheric processes. Nevertheless, due to the limited resources of the future mission, primarily resulting from the considerable distance to Uranus as well as the stringent constraints imposed on the descent probe in terms of mass, volume, and power availability, the study of aerosols could be compromised.
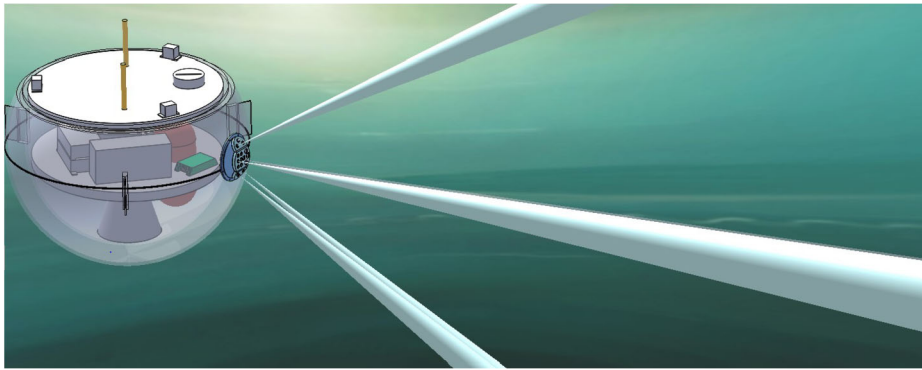
Fig. 1 The Uranus Multi-Experiment Radiometer and its accomodation in the UOP descent probe. The Optical Head is attached to the external wall of the vessel (in blue) and the Processing Electronic is included in the internals of the probe (green). Some of the Fields of View of different optical channels are shown as examples. Credits: Ahmad Alromeadheen for the artistic view of Uranus's clouds background; descent probe inspired by Simon et al. 2021; UMR and final picture composition, INTA

To prevent this significant loss of atmospheric information from Uranus, considering the challenges in developing other future missions to the Ice Giants, and understanding that this kind of science could only be done in situ, we propose the Uranus Multi-experiment Radiometer (UMR) to be included in descent probe of the next mission (see Fig. 1). As will be explained in this work, this instrument concept is simple, compact, flexible, and low-power, with limited controlled mass and volume, offering high scientific yield with minimal resource demand (see a summary in Table 1). Much of its design is based on previous INTA miniaturized instrument developments for Mars devoted to dust and cloud characterization: the Solar Irradiance Sensor (SIS) for the MetNet lander mission (Harri et al. 2017); the Solar Irradiance Sensor (SIS-16), which flew on ExoMars 2016 as part of the DREAMS payload (Arruego et al. 2017; Esposito et al. 2018); the Radiation and Dust Sensor (RDS), which is currently on-board Perseverance as part of the MEDA weather station (Apestigue et al. 2022; Rodriguez-Manfredi et al. 2021); and the Solar Irradiance Sensor 2020 (SIS-20) for the ExoMars 2018 mission (Arruego et al. 2016), integrated into the Meteo Package of the surface platform *Kazachock* (see Zelenyi et al. 2015). This approach allows us to use well-established technologies with a high Technological Readiness Level (TRL).

The UMR incorporates a suite of photodetectors, interference filters, light sources, and optomechanical masks to effectively configure its optical channels, which enables the instrument to capture a range of measurements at different heights, geometries of observation, and wavelength bands. It takes miniaturization as the main design driver, minimizing its impact on the probe accommodation by dividing the instrument into two units. An optical head (UMR-OH), located on the external side of the probe, includes the sensors and the necessary proximity electronics. It can amplify, digitalize, and send the resulting signals to the other unit for electronic processing (UMR-PE), which is located inside. UMR-PE has the ability to control and process the signals. The communication between the two units is carried out using a differential-type serial interface, which utilizes a sealed pass-through between the exterior and interior of the vessel. Then redundant digital serial and power interfaces are used to connect the radiometer to the probe's onboard computer and power subsystems.

Table 1 UMR main characteristics

Parameter	Value
Dimensions	OH: Ø150 mm x 35 mm
	PE: 102 mm x 64 mm x 24 mm
Mass	OH: 350 g
	PE: 220 g
	(Harness not included)
Temperature Environment	OH: 55 K to 110 K
	PE: ∼ 293 K
Radiation Environment	100 krad
Power Consumption	UV-Vis-NIR: 0.75 W (avg.)
	Mid-IR: 1.25 W
	Heater: 4 W
Data rate	33 bytes/s (avg.)
Interface	Redundant RS-422
	@ 57.6 kbps
Structure	>20 bar
Design lifetime	14 years

4 Scientific Objectives

The scientific objectives of the instrument fall into four areas including (1) to study the ultra-violet (UV) energy absorption by aerosols and gases, and determine its penetration in the atmosphere; (2) to study the size, vertical distribution, and optical properties, sources and sinks of aerosols (hazes and clouds) by measuring the scattered sunlight profiles at different wavelength bands, from the visible to the near infra-red (IR); (3) to study the thermal balance of the atmosphere by measuring the up-and-down fluxes from the UV to NIR; and (4) to study the cloud vertical distribution, density and composition at pressures with negligible Sunlight (p > 4-5 bars) by using flash-light emission and detection in the IR.

Table 2 offers an overview of the distinct channel sets assigned to fulfilling particular scientific goals, in addition to those designated for crucial auxiliary measurements. These auxiliary measurements encompass determining the sensor's orientation in relation to the Sun and assessing the potential degradation of channels, for example, due to radiation exposure. The specific placement of each channel within the UMR-OH is visualized in Fig. 2.

4.1 Ultra-Violet Profiles

A basic objective of the instrument investigation is to measure solar ultra-violet (UV) energy deposition in Uranus' atmosphere and its variation with altitude. This will be done using two photodetectors pointing at 90° with respect to the instrument plane (see Fig. 2) and with different UV interference filters (technical description is given in Sect. 5.5). Each photodetector has a field of view (FOV) of 80°, which allows measuring at each altitude the UV radiance coming from almost all directions. To define the dynamic range of the sensors, we will make use of radiative transfer simulations as follows: (1) simulate the sky brightness (radiance field) as a function of the zenith and azimuth angles at different wavelengths

Table 2 UMR channel definition: scientific rationale, wavelength, field of view, pointing, and dynamic range

Channel Type	Scientific Rationale	Channel Number	Wavelength (nm)	Elevation[*] (°)	Field of View (°)	Dyn. Range (mW/m^2)
A	Sun position and trajectory reconstruction	1-4	200-1100	0	120	2775
B.1	Aerosol phase function characterization	5-10	(3x) 560 ± 10	5-10	5	97.62
			(3x) 937 ± 10			45.28
B.2	Spectral Aerosol Optical Depth (AOD) and UV levels	11-14	200-210	0	80	0.144
			285-305			21.8
			690-710			79.5
			990-1010			39.3
C	Energy Balance	15-16	(2x) 190-1100	15-30	$\sim 180 \times 90$	3100
D	Ice species determination and height distribution	17-18	3200-3370	0	80	6.8
			3850-3930			7.2
		IR Lamp	0-4000		40	
E	Displacement Damage Blind-Detectors	19-20	200-1100	N/A	N/A	N/A
			3300			

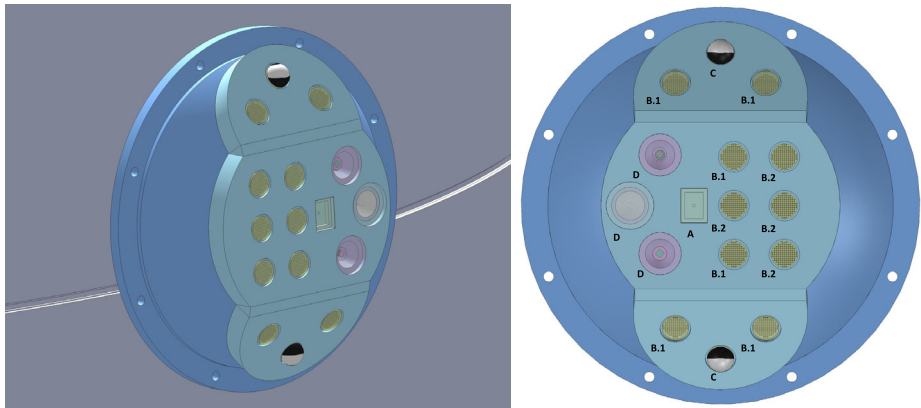[*]With regard to the relative average sun position calculated for the mission

Fig. 2 Schematic design of the Uranus Multi-Experiment Radiometer (UMR). The different channels are identified based on the scientific goals (see Table 2) and operational modes (see Table 5)

and pressures; (2) integrate the radiance field over the sensor FOV and wavelength band to compute the irradiance (units of W m^{-2}); and (3) convert the irradiance into detector photocurrent based on the sensor filters and responsivity (this part is treated in Sect. 6). Figure 3a shows the variation of the sky brightness at p = 0.73 bar as a function of the zenith and azimuth angles simulated using the NEMESIS correlated-k radiative-transfer and retrieval code (Irwin et al. 2008). For these simulations, we used the aerosol/gas model described in Irwin et al. (2022) (referred to as IRW22 thereafter), where the sun is at a zenith angle of 79.1°. By integrating the radiance field over the sensor's FOV and corresponding spectral band at each pressure level, we derive the irradiance expected during the experiment. Fig-
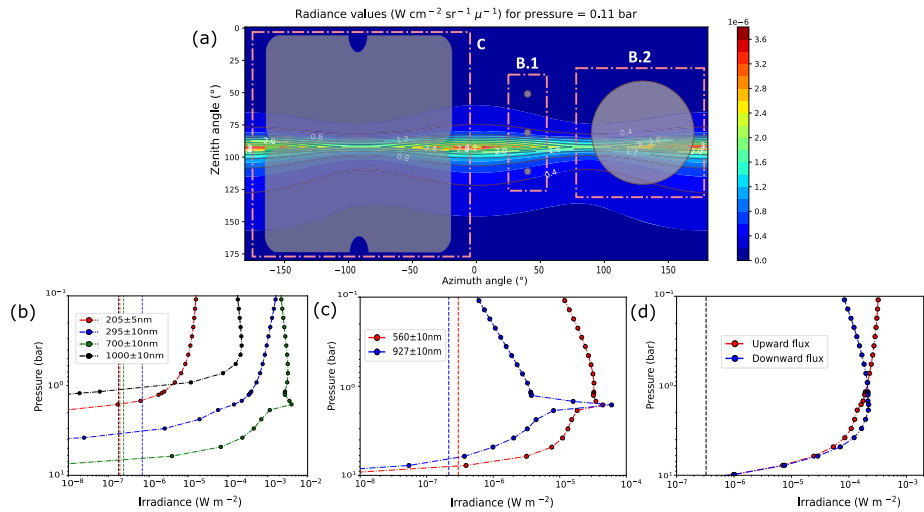
Fig. 3 Simulations of the solar irradiance in Uranus' atmosphere using the NEMESIS code and the IRW22 model. In all the simulations, the solar zenith angle (SZA) is 79.1°. (a) Variation of the sky brightness with zenith and azimuth angles at 0.11 bar level and in the 700 ± 10 nm wavelength range. The transparent-grey circles are added to show the different field of view (FOV) of channels B.1, B.2, and C. (b) Irradiance vertical profiles at 205 ± 5 nm, 295 ± 10 nm, 700 ± 10 nm, and 1000 ± 10 nm for the FOV of B.2 channels and a pointing direction of 70° in zenith angle and 90° in azimuth (concerning the sun azimuth). Corresponding color vertical lines indicate the minimum irradiance level detectable for each channel (see Sect. 0). (c) same as (b) but for channels B.1 560 nm and B.1 937 nm. (d) integrated upward and downward flux for channel C

ure 3b shows, as an example, the irradiance profiles for different spectral bands (specific UV bands have not yet been chosen) and the FOV of B.2 sensors (red circles in a radiance field map Fig. 3a). Thus, by doing this analysis for different sensor orientations (since the probe is likely to tilt and spin during the descent), we can define the dynamic range of each sensor.

Methane dissociation by solar UV and energetic particles leads to a network of chemical reactions that trigger the formation of more complex hydrocarbons such as C_2H_6, C_2H_2, or C_4H_2 (Moses et al. 2018). These hydrocarbons can condense into their respective ices, forming the planet's stratospheric haze. Although methane photolysis and the subsequent haze formation take place in the higher parts of the stratosphere, and thus at altitudes where the probe is not expected to be in measurement mode, questions remain as to whether such processes (formation of photochemical haze) could also occur at deeper levels in the atmosphere. For instance, Irwin et al. (2023) showed that Neptune's dark spots are caused by darkening at short wavelengths of a deep $\sim$5 bar aerosol layer, and one hypothesis is that this dark material is a photochemical product produced by the photolysis of H_2S by UV radiation. Therefore, from these measurements, we will determine the penetration of UV light in the troposphere and establish the altitudes at which the production of photochemical aerosols is possible. Also, by combining these measurements with those made by the channels dedicated to the aerosol (haze and clouds) characterizations (next section), we will determine whether, in a given layer, the decrease in UV radiance is mostly due to the absorption of gases or aerosols. In the following section, it will be explained how these measurements will also be used to constrain the aerosol's optical properties in the UV.

Table 3 Pre-selected detectors for the UMR channels. Manufacturer data for 293 K operational temperature

Detector	UMR Channel	Package	Sensitive Area	Wavelength	Photo-sensitivity	Dark current[*]	Shunt re-sistance Rsh[*]	Noise equivalent power NEP
			(mm^2)	(nm)	(A/W)	(pA)	(MΩ)	(W/Hz$^{1/2}$)
Hamamatsu S5980	A	8.8 × 10.6 mm Ceramic Surface Mount	5 × 5/4 segments	320-1100 (960 peak)	0.72	0.002	–	1.4 × 10-14
Hamamatsu S1337-1010	B.1, B.2, C & E	16.5 × 15 mm Ceramic 2 pin terminals 12.5 mm pitch	100	190-1100[*] (960 peak)	0.5	200	200	1.8 × 10-14
Hamamatsu P16112-033MF	D-E	TO-46	0.7 × 0.7	3270–3330 (3300 peak)	0.0028	–	0.18	1.1 × 10^{-10}
Hamamatsu P16112-039MF	D	TO-46	0.7 × 0.7	3820–3980 (3900 peak)	0.0032	–	0.18	9.5 × 10^{-11}

[*]For reverse voltage $V_R = 10$ mV

4.2 Distribution and Properties of Haze and Cloud Particles

Haze and cloud particles can directly affect the energy balance of Uranus' atmosphere, and thus the atmospheric dynamics, by absorbing and scattering the solar radiation. Different properties of the haze and cloud particles are important for understanding their interactions with solar radiation. The particle size, shape, refractive index, and concentration determine the following aerosol parameters: (1) the phase function (angular distribution of the light scattered by an aerosol); (2) the single scattering albedo (ratio of scattering efficiency to total extinction efficiency); and (3) the optical depth (measure of the extinction of the radiation by the aerosols) of the aerosols.

UMR will derive many of these properties using combinations of spectral irradiance measurements from the UV to the near IR. Six sensors with narrow FOVs (±5°) and at two spectral bands (channels B.1), from 550 nm to 570 nm and from 927 nm to 947 nm, are used to study the aerosol phase function and particle size. To accomplish a wide range of observable scattering angles, each pair of spectral sensors has different pointing angles: 0°, −30°, and 30° relative to the normal of the instrument plane (see Fig. 2) to have zenithal coverage. For azimuthal measurements, the instrument capitalizes on the anticipated tilt and spin of the probe during descent. It incorporates a four-sector sun sensor (refer to Table 2 and Table 3 Channel A) to reconstruct the instrument's attitude. A dynamic model of the descent probe will be developed for this purpose, integrating, at a minimum, data from the sun sensor and the accelerometer included in the selected Atmospheric Structure Instrument (i.e., Ferri et al. 2020). This will ascertain the Sun's relative position to the UMR at all sampling points.

This type of sun sensor is frequently employed for cost-effective attitude determination in low-earth-orbit (LEO) satellites (De Boom et al. 2006), with a precision of up to 0.15° (1σ). It utilizes a quadruple photodetector device (e.g., Hamamatsu S5981), where sunlight reaches the device's center through an aperture or pupil. The section of the aperture and its

distance to the surface of the photodetectors define the solar sensor's field of view (FoV). The signals measured on each quadrant correlate with the Sun's azimuth and elevation (Sun et al. 2023) relative to the sensor's normal. Therefore, this instrument configuration ensures measurements at both small and large scattering angles.

At small scattering angles, the phase function is very sensitive to the particle radius (the larger the particles, the greater their dispersion in the forward direction) and structure (e.g., for aggregates, the slope of the phase function depends on the fractal dimension). Thus, the observations made by B.1 sensors at small scattering angles in the solar aureole will be used to constrain the aerosol particle radius and structure. At backscattering angles ($>90°$), the phase function is very sensitive to the particle shape (e.g., spheres, fractal aggregates, or irregular ice crystals), and this information is key for understanding under which conditions the aerosols are formed at a given altitude. For the retrieval of the phase function, different aerosol shapes and sizes will be employed to study which aerosol model provides the best fit between the observations and simulations. These measurements require a wide sensor dynamic range to cover the range that goes from the low intensities in the backscatter angles to the direct light intensity when the sun is within the sensor FOV. This will be done by using a number of channel gains (see Sect. 0). Figure 3c shows irradiance profiles simulated for channels B.1. As for the UV sensors, the definition of the dynamic range will come from the radiative transfer simulations.

In addition to B.1 channels, two more sensors, pointed normally to the sensor, with 80° FOVs, and spectral bands of 700 ± 10 nm and 1000 ± 10 nm will be used for the aerosol retrievals (last B.2 channels of Table 2). The analysis of these sensors' measurements, along with those from the UV sensors, will provide information on the optical depth and single scattering albedo at four spectral bands. Because of their wide FOV, their observations are less affected by the phase function than the B.1 channels, being the aerosol total opacity and single scattering albedo as the main parameters controlling their measurements. The spectral aerosol opacity and single scattering albedo depend on the particle radius and refractive index. Thus, the aerosol properties and vertical distribution will be retrieved by using combinations of the B.1 and B.2 channel measurements. This implies that both B.1 and B.2 channels must operate simultaneously during the descent and up to 1-2 bar level.

4.3 Solar Net Flux

As one of the objectives of the UMR is to directly estimate the heating rates in Uranus' atmosphere, the instrument has two photodetectors looking upward and downward to measure the solar flux in the spectral band from 190 nm to 1100 nm. The detectors are pointing upwards and downwards with a FOV that covers about 180° in azimuth angles and about 90° in the zenith (channels C, see Fig. 2) using a masked diffuser. Due to the parachute's blockage and the fact that the instrument is designed to be on one side of the probe, these measurements cannot cover all the zenith and azimuth angles. However, they are captured through successive samples as the probe rotates.

The net flux is computed from the difference between the downward flux and the upward flux, and the difference in the net flux at the up and down boundaries of an atmospheric layer gives the solar energy absorbed by it (heating rate). Thus, from these measurements, the planet's heating profile can be directly estimated. This information is key for understanding the role of hazes and clouds in the stratosphere and troposphere energy budgets.

Before using these measurements, three corrections need to be made: (1) extending the range from 190 nm to 1100 nm to 190 nm to 2500 nm; (2) combining different observations to cover the whole range of azimuth angles and compute by RT simulations the intensity at

the angles masked by the parachute; and (3) correct for the tilt of the sensor plane with respect to the horizontal. For these corrections, we will use the NEMESIS code and the IRW22 aerosol/gas model (but using the aerosol profiles derived from B operational mode (see Table 1)). Figure 3(c) shows the upward and downward fluxes simulated using the IRW22 model. Based on these simulations and the dynamic range of the sensors (see technical description in Sect. 5.5), these measurements are expected to cover the altitudes between the lower stratosphere (specific altitude conditionate to the aeroshell removal) and the 4-5 bar level in the troposphere.

4.4 Deep Clouds Composition and Density

Clouds on Uranus can be of different composition depending on the altitude where they form. Different images of the planet have revealed the presence of discrete clouds at different locations and time periods (e.g., Karkoschka 2001). Based on the altitude of these clouds (near or above the 1-2 bar level) and the saturation vapor pressure curves of several possible condensates, it has been inferred that the composition of these clouds is methane ice. Below the methane condensation level, at pressures ~ 5 bars, different radiative transfer analyses of observations in the visible and IR have shown the presence of a cloud layer (referred here to as the main cloud deck) that, contrary to the methane clouds, seems to be present at all latitudes and periods of time. Irwin et al. 2018 and 2019, reported the detection of gaseous H_2S above the main cloud deck, and based on these results, they argued that the principal constituent of this cloud is likely to be H_2S ice. Most recently, Irwin et al. 2022 found that the main cloud deck is actually composed of a mix of haze and CH_4 ice at 1-2 bar, and that below this there is a deeper cloud of haze and H_2S ice at p $> \sim 5$ bar. The existence of H_2S at these levels implies that the abundance of H_2S exceeds that of NH_3 above the water condensation level, which leads to the expectation that deeper than ~ 10 bar there exists a cloud of NH_4SH, followed at even deeper levels by a cloud of H_2O (Carlson et al. 1988). However, our limited knowledge of Uranus' atmosphere at pressures greater than ~ 5 bar, where sunlight intensity is very low or negligible, makes it complicated to establish what the cloud structure and composition are at these pressures.

To study the cloud structure and composition below the 1-2 bar level, channels D of UMR consist of one IR light lamp in the range from 2 μm to 6 μm, and two detectors with photosensitivity in the range of 3.20-3.37 μm (channel 17 in Table 2, Ch-17 in Fig. 4 (b)), and 3.85-3.93 μm (channel 18 in Table 2, Ch-18 in Fig. 4 (b)). When the probe is within a cloud layer, the light emitted by the lamp is scattered by the cloud particles and part of it is received by channels 17 and 18. The number of photons received at each band depends on the cloud composition, opacity, and particle radius. Figure 4a shows the spectral extinction and scattering cross sections of spherical particles made of CH_4, H_2S, and NH_4SH ice with an effective radius of $r_{eff} = 2$ μm. Here we see that when the cloud is made of H_2S, the intensity in channel 17 is expected to be greater than that in channel 18. On the contrary, if the cloud is made of NH_4SH ice, then the intensity in channel 18 is expected to be greater than in channel 17. Note that although CH_4 ice also displays an absorption feature in the IR lamp range, the absorption feature is given at a strong CH_4 gas absorption band, making the identification of CH_4 ice difficult.

A number of simulations using a Monte-Carlo radiative transfer code (Toledo et al. 2017, 2023) were performed to define the dynamic range of channels 17 and 18. In these simulations, the photons are emitted from a singular source (the lamp) and collected by a bin next to it whose area is equivalent to the detector's. Figure 4b shows simulations of the variation of the photons received with wavelength for a detector with a radius of 0.35 mm, and for
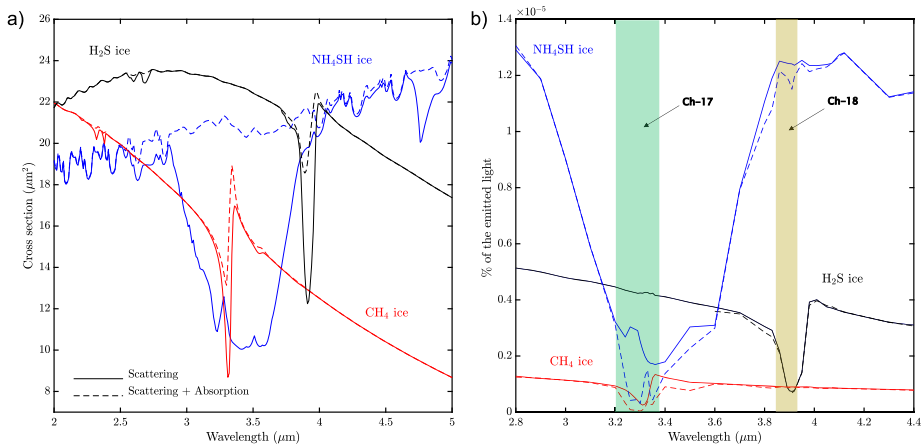
Fig. 4 (a) Cross section of CH_4, H_2S, and NH_4SH ice particles with an effective radius of 2 μm computed using Mie theory and the refractive index given in (Howett et al. 2007; Schmitt et al. 2012). (b) Monte Carlo simulations of the photons scattered and absorbed by clouds made of CH_4, H_2S and NH_4SH ice. The photons are emitted from a source that is next to the detector (radius of the detector: 0.3 mm). In all the cases, the cloud opacity and r_{eff} are 1 km^{-1} and 2 μm, respectively. The dashed lines represent the simulations when CH_4 gas absorption is included and the solid ones when it is not. The colored rectangles indicate the wavelength range of channels 17 (green) and 18 (light brown)

different cloud compositions. In all the simulations, the cloud opacity and effective radius are fixed to 1 km^{-1} and 2 μm, respectively, and methane gas absorption was included using the mole fraction retrievals given in Irwin et al. (2022). Here we see that while the methane ice absorption feature is masked by the methane gas absorption, the presence of NH_4SH and H_2S ices in the atmosphere can be determined by using the intensity measured in channels 18 and 19. Thus, from these measurements, we can constrain the opacity and r_{eff} of the clouds (the greater the opacity, the greater the intensity measured in both channels), and discriminate between NH_4SH and H_2S ice (from the ratio between intensities). Based on simulations similar to those shown in Fig. 4b, the dynamic range of channels 17 and 18 is defined to operate between 1 and 10 bars. This will allow us to study the cloud structure and composition at altitudes where our knowledge of the atmosphere is extremely limited.

5 Instrument Design

5.1 Mission Overview and Environmental Requirements

The Uranus Orbiter and Probe study (Simon et al. 2021) encompasses various inputs that have been used in the mission's design and assessing its feasibility. Clearly, not all the technical prerequisites essential for the detailed design of its payloads are documented, but it is possible to glean the key considerations for its development.

First and foremost, this is a 13-year interplanetary journey mission, with a probable Jupiter flyby for gravitational assistance and power sources used based on radioactive compounds (both in the orbiter and the probe). Consequently, the accumulated radiation during the trip is a significant design requirement when selecting electronic and optical components. A minimum Total Ionizing Dose (TID) resistance of 100 krads (for an equivalent

Aluminum protection of 6 mm) has been established in the UPO study. Additionally, standards of quality and reliability have been set for all materials and components to meet the mission's longevity requirements (Level 2 EEE parts selection in accordance with EEE-INST-002, Sahu et al. (2003)).

Furthermore, in the vicinity of Uranus, stringent thermo-mechanical requirements will be imposed on the probe. Firstly, during the phase that starts with the separation of the probe, and ends with its insertion into the atmosphere, referred to as the 60-day probe coast phase. When the insertion phase of descent starts, the probe is encased within an aeroshell, allowing it to enter into the planet's atmosphere at high speed. After the initial braking, a small parachute is deployed to generate mild drag, facilitating the release of the front part of the aeroshell, exposing a significant portion of the probe to the atmosphere at 0.1 bar. Subsequently, the upper part of the aeroshell is released, and a second parachute is deployed, enabling a gentle descent over approximately one hour, until it reaches a pressure of 10 bars, marking the conclusion of the mission. Throughout this period, the outer surface of the probe will be exposed to the frigid temperatures of Uranus' atmosphere (55 K – 100 K). Additionally, the probe's exterior will experience mechanical stresses induced by atmospheric winds and, notably, the exponential increase in pressure during the descent.

The proposed design for the probe (Simon et al. 2021) addresses these requirements by employing a structure consisting of two concentric vessels separated by aerogel for thermal insulation. The inner capsule houses the batteries, platform hardware, and scientific payloads. Radio-isotope Heater Units (RHUs) are strategically placed inside to maintain the interior temperature at a comfortable 293 K, while a thermally coupled radiator at the rear of the aeroshell assists in heat dissipation. This design ensures the probe's survivability in the face of extreme temperature variations. Related to the structural design, to prevent pressure-related issues and optimize the probe's weight, a venting valve is utilized, allowing for the gradual equalization of the differential pressure between the interior and exterior to a maximum of 1 bar, permitting a controlled ingress of air into the interior, that makes that the instruments inside or the components have to withstand at least 10 bar of pressure.

5.2 Probe Accommodation

Our instrument concept based on the two-unit configuration provides great flexibility in terms of accommodation. It avoids the need for the use of large drills in the vessel that will strongly impact the integrity of the probe's mechanical structure and mostly, in the thermal subsystem due to the possible power leaks.

The UMR has just one accommodation requirement: the UMR-OH structure's plane must be perpendicular to the sun's relative view (see Fig. 1). The angular distance between the lateral sensors concerning the direct solar path, and the tilt and rotation of the probe during descent, ensure the sampling of small angles between the sun position and the sensors pointing direction. An adaptation braze, similar to the ones described for the Venus probe's instruments (Bienstock 2008) will be designed once the final position of UMR-OH is determined.

5.3 Mechanical Design

The mechanical design of the UMR, as mentioned earlier, consists of two units (see Fig. 5a&b). The internal unit, UMR-PE is simple, sufficient to accommodate 2 electronic boards, and supports the electrical and mechanical interfaces with the probe. Its design can be adapted to meet the accommodation requirements of other components, allowing it to
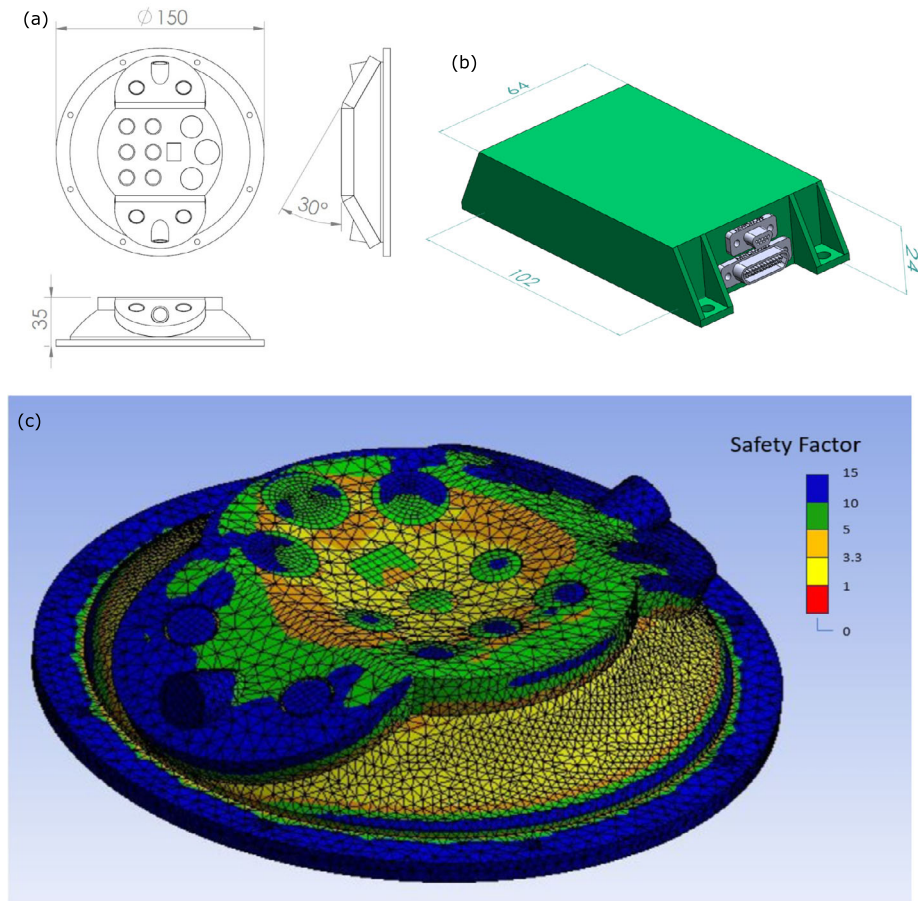
Fig. 5 (a) Main dimensions (mm) of the UMR-OH. (b) Same for the UMR-PE. (c) Preliminary structural analysis for 20 bars of external pressure applied to the UMR-OH. The color scale corresponds to the safety factor. The deformation is exaggerated to observe its effects

be integrated into various possible solutions: racks shared by instruments, mechanical interfaces on other devices, etc. The structure of the exterior unit, UMR-OH, uses a semi-spherical shape as the basis for its construction, truncated in three planes to obtain the three required observation angles. This shape was chosen for its structural optimality as well as its soft aerodynamic profile.

Both structures contain a custom valve that allows the internal air to be evacuated during launch, leaving it in a vacuum throughout the rest of the mission. Therefore, the structure has been designed in such a way that it can withstand at least 20 bars. The results of a preliminary strength analysis are shown in Fig. 5b, where we can observe that the structure is capable of withstanding this stress with a safety margin higher than 1.

5.4 Thermal Design

The thermal design will ensure that the instrument's internal elements remain within the allowable temperature range throughout the different mission phases, namely from launch and
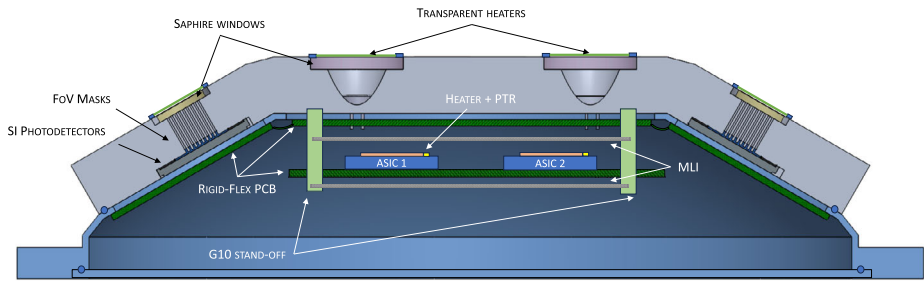
Fig. 6 Radiometer Optical Head section. Optomechanical (black labels) and Thermal Design (white labels) details have been highlighted

interplanetary cruise, to the probe coast, entry, and descent. The design relies mainly on the ability of most of the parts to survive/operate at cryogenic temperatures. Some components require nonetheless of thermal conditioning, which is provided by active heating coupled with passive insulation.

In the UMR-OH, the optoelectronic detectors and IR lamp are mounted on a flexible PCB (Printed Circuit Board) tailored to fit the main body of the radiometer (see Fig. 6). Every channel is covered by sapphire windows on top and the whole assembly is intended to operate at the environmental conditions of each phase, and therefore all its components are subjected to qualification for operation at temperatures up to 35 K (55 K less margins). Currently, this family of photodiodes has been qualified for the harsh Martian environment through an extensive test called the Package and Qualification Test (PQV), in which all RDS devices were subjected to over 3000 thermal cycles ranging from 138 K to 323 K. Furthermore, in a first step to the aforementioned qualification, a reduced test was conducted at INTA's cryostat in July 2023, where 2 ASICs (Application Specific Integrated Circuit) and 6 photodiodes were exposed to cryogenic temperatures for 15 days (35 K – 100 K), with no degradation observed in the optoelectronics devices (dark current and final visual inspection).

A PCB with the head main electronics is located in the middle of the UMR-OH, with two ASICs devices as critical elements in terms of temperature limitation. In the thermal testing at INTA's cryostat, it was demonstrated that they can survive (non-operational) and operate (digital part) at temperatures up to 35 K. However, a lower design limit of 120 K (100 K with margins) is imposed for the correct operation of both the digital and analog parts.

A heater (4 W peak) working in a closed loop is placed on the ASICs and used to warm up the components prior to the switch-on. To reduce the amount of heat required, the PCB-E is conductively decoupled from the UMR-OH structure through G10 standoffs. In addition, this rigid PCB is enclosed by a low emissivity SLI to reduce radiative losses (see Fig. 6). A platinum resistance temperature detector (RTD) is used to provide the input for the temperature control (e.g., Lakeshore PT-111).

During the interplanetary cruise, the probe instruments are supposed to be powered by the main spacecraft. Once in Uranus, the probe release from the orbiter is followed by an approximate 60-day coast, in which the Descent Module relies only on its primary batteries for electrical power and internal RHUs for survival heating. During this phase, the external environment of the UMR-OH consists of the probe aeroshell, whose inner face temperature is estimated to be around 55 K. The UMR-OH will remain switched off during this phase and it is intended to withstand such low temperatures during the whole coast. Note that thanks to the low-temperature qualification of the UMR-OH components, it can survive the coast phase without the need for internal heating or funneling heat from the probe RHUs.

Fig. 7 Power profile for the UMR-OH mission, consisting of a warm-up period of ~ 30 minutes before enter into the Uranus atmosphere and then, a nominal operation period for ~ 1 hour (a). ASIC temperature for both periods, warm-up and nominal operation (b)
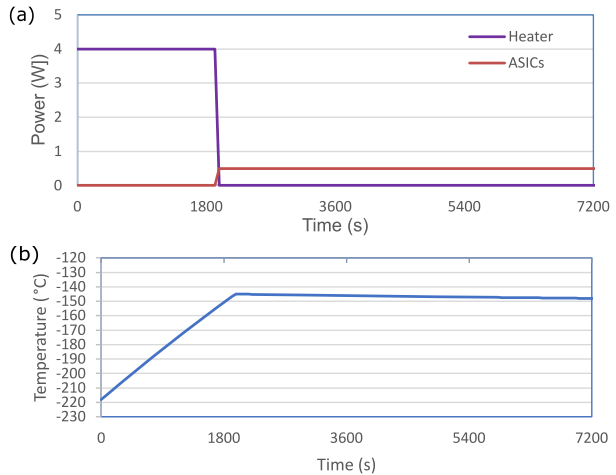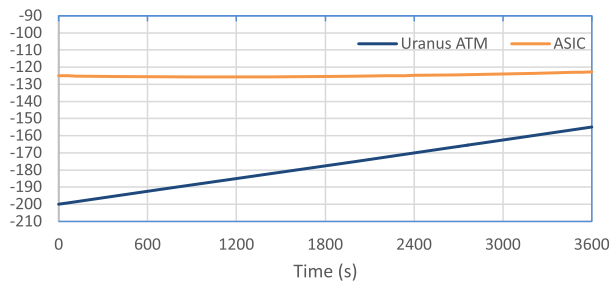

Fig. 8 Uranus atmosphere and ASIC temperatures during 1 h descent (nominal period) science phase

The instrument is foreseen to be switched on before the entry (see Sect. 6). Beforehand, the ASICs are warmed by the (4 W) heater for approximately 30 min (~ 2 Wh, see Fig. 7) until its minimum operational temperature (120 K) is reached, to ensure a safe switch on.

The probe heatshield is released around 120 seconds after starting the planet entry. After the aeroshell separation, the Descent Module and hence the UMR-OH are directly exposed to the Uranus atmosphere. The probe descent to 10 bars lasts for around 1 hour. During this phase, the instrument is ON and the electronics self-heating (~ 0.5 W) keeps the ASICs temperature above the required limit (see Fig. 8).

Note that since the UMR-OH is hermetically sealed, the internal cavity will remain in vacuum, i.e., there is no external cold air inlet during the descent phase, hence avoiding also the additional heat losses due to the gas conduction.

5.5 Optoelectronic Design

The optoelectronic design of several channels uses silicon detectors (Table 2 A, B, and C sets). It is primarily based on the same approach that was used for the RDS (Apestigue et al. 2022; Alvarez-Ríos and Jiménez 2017) which includes: (i) silicon photodiode with a spectral range from 190 to 1100 nm; (ii) interferential filters developed ad hoc for the instrument and mounted directly on top of the detector substituting its original quartz window; (iii) FoV masks made by one (Table 2 A set) or multiple cylinders with ratios diameter/length corresponding with the intended angle of vision (Table 2 B and C sets); and (iv) a sapphire window to protect the interior of the UMR from the Uranus atmosphere.

Since the irradiance reaching the planet is almost 160 times less than that reaching Mars, a detector model with nearly 100 times more active area has been chosen to capture a greater amount of light (Hamamatsu S1337-1010bq) for B and C sets. However, this increases the device's dark current could potentially compromise the dynamic range, but this effect is nearly insignificant when operating at such low temperatures (50 K-100 K). In the case of A set, we have selected a segmented device with 4 photodiodes in a 2×2 configuration. The orifice of its FoV mask collects the light as a beam in the middle of the device if the Sun's path is normal to its surface. The four sensors receive the same light in this configuration. When the instrument turns, the light spot over the detector will move and modify its shape. The relationship between the 4 sensors signals will be used to calculate the relative position between the instrument and the Sun. The diffuse light could introduce some error in this attitude determination but it is estimated that the precision could be around 1° both azimuth and zenith.

Similarly to what occurred in the Mars mission design, these components may experience degradation due to exposure to radiation during the lengthy journey to Uranus, stemming from the damage caused by energetic particles and cosmic rays. Consequently, a shielded photodiode has been incorporated, and its dark current is measured to assess potential degradations across the various channels.

On the other hand, the spectral transmittance of these devices will need to be thoroughly characterized, as low temperatures alter the properties of silicon, modifying its internal absorption and refractive index (Nagakubo et al. 2015). Additionally, carrier mobility is also reduced under these conditions, and the combination of these two factors results in a decrease in responsivity with temperature (Camin and Grassi 2006). In the study by Glebov et al. (2018), they analyze this effect in pre-selected photodiodes by UMR (S1337-1010BQ), obtaining responsivity losses of less than 6% for spectral bands at 900, 700, and 500 nm. However, they indicate that at 1000 nm, losses can reach up to 60% at 90 K.

For the IR channels (Group D), we have pre-selected new photodetector devices, Indium Arsenide Antimonide (InAsSb), from the Hamamatsu family P16112-XXMF (see Table 3). This detection technology is uncooled and highly sensitive. The devices in this family include band-pass filters centered, among others, at 3.3 um and 3.9 um, which align perfectly with the scientific requirements for detecting and characterizing clouds (see Fig. 9a).

Different types of InAsSb structures have been tested for both ionizing and non-ionizing radiation effects. Superlattice structures appear to be quite robust (Steenbergen et al. 2013), but barrier architectures exhibit degradation in quantum efficiency (Morath et al. 2019). As a tentative selection, a corresponding qualification campaign for radiation and cryogenic temperatures will be conducted on these devices (among others equivalent candidates) in the subsequent stages of our technological UMR development program.

For the case of the IR emitter, we have pre-selected a nichrome (NiCr)-filament-based lamp (INFRASOLID HIS2000R-A300-6), that offers a high-optical-power emission (up to 620 mW, see Fig. 9 (b&c)) in a very compact device (Table 4). It includes a gold-plated reflector that offers enough narrow angular radiation emission and a sapphire window that closes the hermetic TO-8 package.

All sapphire windows used for protecting detectors and emitters should include a heater (see Fig. 6) to prevent potential condensation of species that reach their dew point (e.g., CH4, H2S) during descent. The aim is to slightly heat the external surface of the windows above the atmospheric temperature, as suggested in previous instrumentation for descent probes (e.g., Sromovsky et al. 1992; Ragent et al. 1992). To achieve this, we propose using an Indium tin oxide-based coating (ITO) on or below them. These materials are commercially used as transparent heaters in the UVA-NIR region of the light spectrum.

Table 4 Pre-selected IR lamp for the UMR channels. Manufacturer data at operation temperature of 293 K

IR Lamp	UMR Channel	Package	Radiating element area	Wavelength	Optical output power	Electrical power	Electrical resistance	Modulation frequency
			(mm^2)	(µm)	(mW)	(W)	(Ω)	(Hz)
Infrasolid HIS2000R-A300-6	A	TO-8	40	2-6	620	2.5	5-6	4-10[*]

[*]50%-20% modulation depth
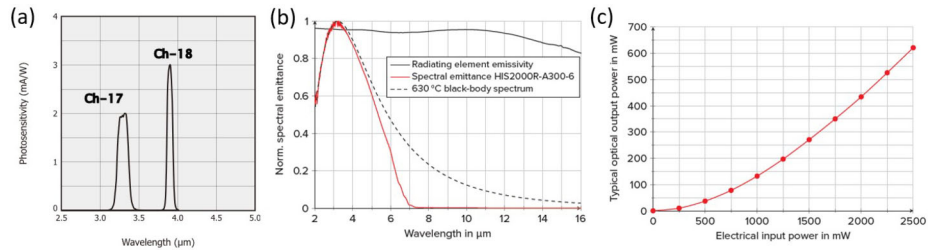
Fig. 9 (a) IR selected sensors family wavelengths. (b) IR lamp emission spectrum and (c) optical power emission. Credits: component datasheets

INTA has a solid track record in using this coating for space applications. The institution developed the liquid-crystal variable retarders included in the Solar Orbiter SO/PHI (Solanki et al. 2020) and METIS/COR (Antonucci et al. 2020) instruments. These devices use ITO-deposited films for liquid-crystal active control (Alvarez-Herrero et al. 2011) and have consequently been qualified for the space environment (Alvarez-Herrero et al. 2017). For mid-IR detectors, we plan to explore the use of ITO coatings doped with other compounds (e.g., ZnO or Zn) that could enhance Mid-IR transmittance (Genty et al. 2011), where traditional ITO coatings exhibit absorption behavior. Preliminary calculations indicate that we will need 25 mW to prevent condensation on each window, totaling 400 mW of power during the 1 h descent phase.

Another potential cause of channels degradation could be the deposition of particles on the protection windows (which are expected to be predominantly ice crystals). In this regard, a fluid dynamic study will be conducted to evaluate different designs of the OH shape and windows integration, or even to include deflection surfaces in order to minimize this effect, which will need to be characterized on Earth by means of wind tunnel facilities.

5.6 Electronic Design

5.6.1 Optical Head – UMR-OH

INTA has maintained a collaborative partnership with the Institute of Microelectronics of Seville (IMSE) for over 15 years, focusing on the development of mixed-signal ASICs for space use and extreme temperature conditions. During these years, IMSE has developed its own radiation-hardened libraries for the standard AMS CMOS 0.35 µm technology (Ramos-Martos et al. 2012 and 2013). These libraries employ design hardening techniques
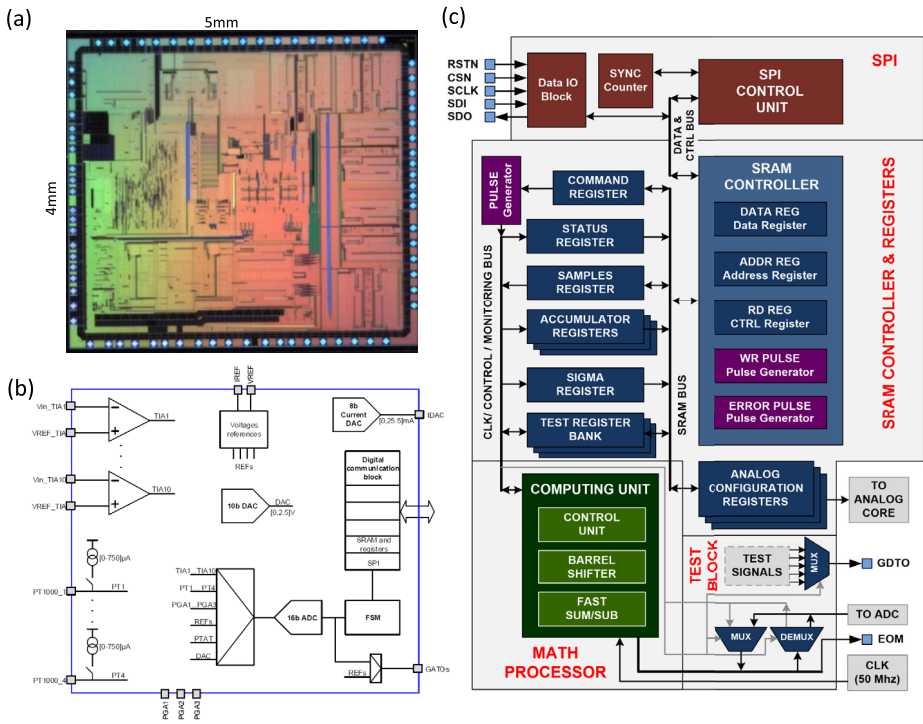
(a)

(b)

(c)

Fig. 10 (a) SIS20 ASIC physical dimensions and layout. (b) SIS20 ASIC Functional Blocks. (c) SIS20 ASIC Digital Block in detail

(Sordo-Ibañez et al. 2014) both to mitigate the effects of radiation and to use it at low temperatures (323 K − 148 K). IMSE has also qualified the encapsulations for these developments, compatible with MIL-STD-883 standards and with extreme thermal cycling through long-duration PQV (Package and Qualification Verification) tests. This effort has allowed the institute to develop the ASIC for the wind sensors (WS) of the MEDA meteorological station, which currently operates in the harsh conditions of the planet Mars.

For the ExoMars 2018 mission, a mixed-signal ASIC (Vázquez et al. 2018) was developed for INTA's radiometer, the Solar Irradiance Sensor 20 (SIS-20). This ASIC could not undergo radiation testing, but it shares the same building block that was previously tested. Therefore, it can be inferred that it exhibits the same radiation-hardened behavior (Ramos-Martos et al. 2012 and 2013): (i) the technology and library were tested up to 318 krad (Si) for total ionizing dose (TID); (ii) it is single event latch-up (SEL) free up to 81.8 MeV·cm2/mg (heavy ions); (iii) it is single event transient (SET) free up to 40 MeV·cm2/mg; and (iv) it is single event upset (SEU) free up to 22.5 MeV·cm2/mg.

This latter development has been taken as a starting point for the electronic design of the Optical Head unit of the UMR (UMR-OH).

The main components of the UMR-OH electronics are a pair of mixed ASICs previously developed for the SIS-20 radiometer (Vázquez et al. 2018). This device, Fig. 10 (a), comprises four major subsystems (Fig. 10 b) summarized in: i) an analog front-end that includes 10 trans-impedance amplifiers (TIAs) with two programmable gains per channel, 4 PT1000 platinum resistance channels, an 8-bit current-output DAC for driving light calibration sources like LEDs, and 3 general-purpose voltage amplifiers with configurable gain; ii)
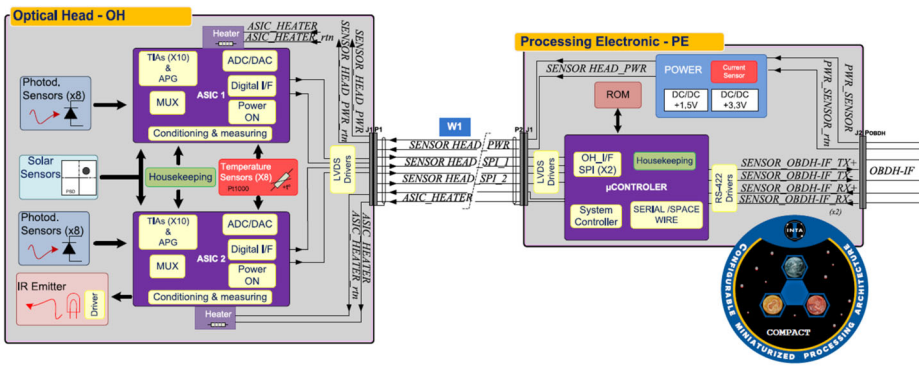
Fig. 11 Electrical functional blocks detail of the two units that comprise the UMR

a 16-bit ADC with multiplexed input and a preceding instrumentation amplifier with configurable gain; iii) a 10-bit DAC used as an input to the previous instrumentation amplifier, providing sub-ranging capabilities; and iv) a digital layer, as depicted in Fig. 10 (c), that encompasses digital signal processing blocks enabling various automatic functions such as oversampling up to 256 samples averaging, standard deviation calculations, a 100 Kbits/sec slave SPI interface, configuration/control registers, a Power-on-reset (POR) circuitry, and a CLK signal generator.

As discussed in Sect. 4, to achieve the scientific objectives, the UMR employs 20 optical channels integrated into the OH. To maximize integration, we use two of these ASICs (see Fig. 11). This approach allows for a high degree of integration by automatically conditioning and digitizing the data with a power consumption of 250 mW each.

The conditioning of both the Si photodiodes and the InAsSb photodetectors is based on a solution in the designs of both RDS and SIS-16 (see Fig. 12 (a)). In this scheme, the first trans-impedance stage contains the main amplification that provides the dynamic range for the optical channels. This first stage allows for configuring two gains, adapting the range to measure low values of scattered diffuse light intensity or, conversely, for situations where direct sunlight may enter the FoV, causing possible saturation. A second stage is added to the analog chain, including an instrumentation operational amplifier in combination with a DAC. This configuration allows the application of sub-ranging techniques to maintain high levels of accuracy when changing the main gain. This stage also provides a final gain to the result of the subtraction configurable with 1 or 50 amplification factors.

Due to the fact that measurements are performed at low frequency, the required amplification levels can be achieved with the first transimpedance stage without bandwidth limitation. The dynamic range is calculated based on simulations obtained with the radiative transfer model (last column Table 2), for worst cases with the sun inside the FoV. This amplification levels necessitate the use of feedback resistances (Fig. 12(a) Rf1 and Rf2) with very high values (from mega to giga ohms), making thermal noise in these resistances dominate over the electronic noise of the amplifier. In Fig. 12(b), we present an example of calculating the signal-to-noise ratio (SNR) as the ratio of the current required by the photodiode to the current noise calculated. The last is calculated as the root mean square sum of three terms: (i) the thermal noise from the feedback resistance Rf; (ii) the thermal noise of the intrinsic resistance of the photodiode R_{shunt}; and (iii) the shot noise resulting from the photocurrent received by the photodetector and its dark current (at worst case mission operational temperature of 120 K).
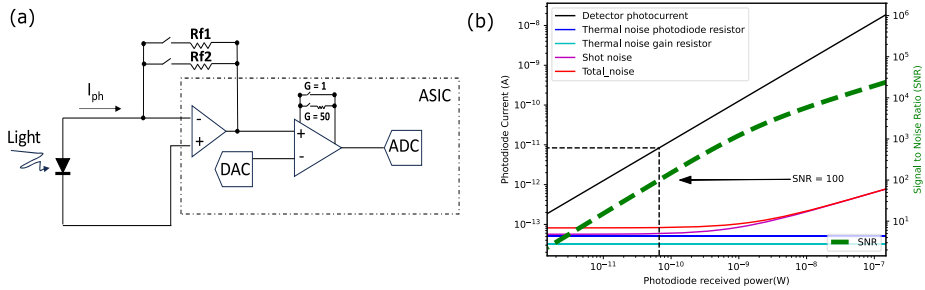
Fig. 12 (a) UMR photodetectors acquisition chain shematics. (b) Example of noise levels calculations for each detector. In this case, we analyze channel 11 (B.2 UV) with corresponds to the limit of detection (vertical line) associated with this channel in Fig. 3 (b)

To infer the minimum irradiance level for each channel, limited by the noise, we have established SNR = 100 as a lower limit (Fig. 12 (b)). With the corresponding received power at the receiver, considering its effective active area (accounting for losses due to filter transmittance and FoV masks), we have calculated the minimum irradiance levels for each of the channels. These can be observed as vertical lines in Fig. 3 (b), (c), and (d).

In the case of mid-infrared (mid-IR) channels, a scheme identical to that of Si photodiodes will be employed. In this context, the emphasis is on the faint signal derived from the backscattering of aerosol particles when illuminated by the lamp. Noise calculations analogous to those for the Si photodiodes have been conducted for these devices, but in this instance, the minimum and maximum received light power from the scattering of the lamp light (Fig. 4 b) are taken as input. For Channel 17, we obtain a signal-to-noise ratio (SNR) ranging from 29 to 200 for the minimum and maximum expected received power (which depends on the species present during the measurement). For Channel 18, we have obtained an SNR ranging from 20 to 271 in a similar manner. Both results could be enhanced using the ASIC oversampling capability, which could rise theoretically the SNR up to a x16 factor (for 256 samples) with a conversion time of 377.5 ms.

To mitigate background noise that may arise from the atmosphere and even from the channel housing, and to filter the desired signal, a digital lock-in filter will be implemented. Due to the high levels of amplification required, the source will be excited at the order of tens of hertz, and the ASIC will be responsible for generating the carrier by driving a power driver that controls the lamp. Additionally, the ASIC will digitize the signals and provide them to the microcontroller, which will handle the processing tasks. Besides eliminating background noise, this technique can also be employed to enhance potential secondary amplification. Once the signal is converted to voltage through the initial transimpedance stage, the second amplification is conducted in voltage, and thus, the 1/f noise from the operational amplifier becomes significant. Utilizing a filter with a 10 Hz carrier can mitigate this noise by a factor of 5, depending on the operational amplifier's characteristics. However, the final frequency selected shall have a compromise between the IR-lamp operational frequency capability, the oversampling selected in the ASIC and the final acceptable SNR figure.

To accommodate all these electronics, the UMR-OH has four boards linked together forming a unique rigid-flex polyamide PCB. Two of them are close to the upper structure that supports the three lateral photodetectors (B.1 and C sets). The central rigid PCB supports the B.1 and B.2 photodiodes, the solar sensor (A set), and the IR lamp and photodetectors (D set). Finally, at the bottom of the set, we have the main PCB that contains the ASICs and the driver for the lamp.

5.6.2 Processing Electronic Unit – UMR-PE

The UMR-PE is equipped with two electronic boards that serve for two primary functions: (i) to adapt the power levels provided by the platform and (ii) to accommodate a small payload computer. This design is based on the COMPACT architecture (Configurable Miniaturized Processing Architecture) developed by INTA (Martin-Ortega et al. 2017). The basic idea of the COMPACT approach is the recursive employment of several components with predefined configurations, allowing for the customization of an optimal computer for each application based on its specific requirements, including computational capacity, performance, power consumption, and footprint. Consequently, this architecture employs various devices for power conversion, such as isolated DC-DC converters and linear regulators, as well as different components for signal processing and coprocessing, including microcontrollers and FPGAs. COMPACT components are chosen based on their radiation resistance and undergo testing to ensure their performance at low temperatures avoiding the use of heaters. In the framework of COMPACT, various base configurations have been predefined depending on the system to be controlled, with the simplest configuration for the UMR consisting of a microcontroller paired with an external program and massive data storage memory (Fig. 11).

The selected microcontroller for UMR is the SAMRH707. It is a RadHard device (100 krad; LET > 78 MeV·cm^2/mg) based on the ARM Cortex M7 architecture developed by Microchip, capable of reaching up to 100 DMips of processing power. It comes equipped with its internal memories, including 128 kbytes of Flash, 320 kbytes of SRAM, and 128 kbytes of ROM. It offers a wide range of communication peripherals, including high-speed (SpaceWire), and advanced analog features: a 12-bit ADC and DAC. Additionally, it includes numerous low-power modes, allowing for fine-tuning of its computational capabilities in response to energy demands. For the UMR, using a 10 MHz clock, the maximum nominal power consumption would be 400 mW with a sleeping mode of ~1 mW.

The use of a microcontroller instead of low-resource anti-fuse FPGAs, as in our previous radiometers (SIS, SIS-16, RDS, and SIS-20) represents a significant advance in flexibility and capabilities for the UMR. This transition offers advantages ranging from the ease of hardware development and testing during the design phases to the expanded capabilities that can be imparted to the instrument. These capabilities include independence from its operation concerning the central computer, the ability to perform in-flight floating-point calculations, and the application of compression algorithms to telemetry data, among others.

6 UMR Operational Modes

The UMR has been designed to meet various scientific objectives, and as a result, it incorporates different sets of sensors to achieve them. Consequently, these sensor sets operate in distinct ways throughout the mission, depending on the specific phase. We refer to these distinct operational states as Operational Modes (OPM). For each OPM, it is crucial to determine which channels need to be activated, identify the required housekeeping signals, and establish the specific sampling frequency necessary to meet the scientific objectives, including factors like vertical resolution and azimuthal data. Armed with this information, we can then estimate the amount of data needed throughout the mission and the corresponding energy consumption for each scenario. Table 5 summarizes these estimations for the UMR and permits comparison with the UOP mission (Simon et al. 2021).
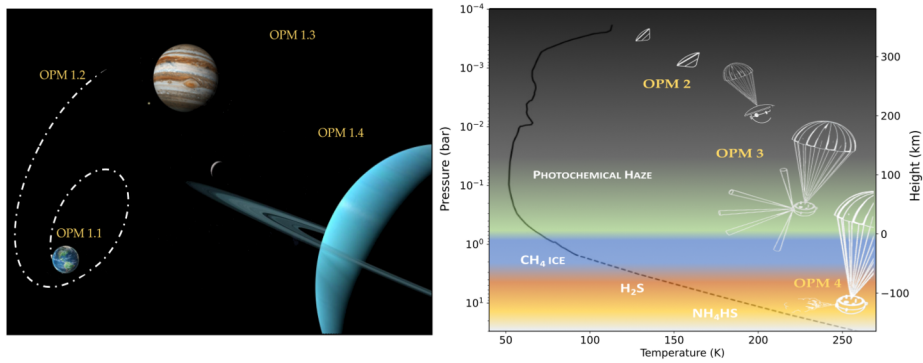
Fig. 13 Mission Operational Modes by mission stages: (a) interplanetary trip, (b) during the probe descent over Uranus atmosphere

For the 1-hour whole mission, the UMR generates 161.9 kilobytes of raw data (Table 5), which represents 7.5% of the total data budget for the entire probe (2.3 megabytes or 17 megabits as per Simon et al. 2021). Using, for example, the same delta-encoding compression algorithm used in MEDA for the RDS (Rodriguez-Manfredi et al. 2021), these figures could be reduced by 55%. Regarding energy consumption, only 2.3% (2.75 watt-hours) of the 121 watt-hour probe's energy budget would be used by our instrument, which is a negligible amount in total.

The different operational modes are described below:

OPM 1: This operational mode encompasses four checkouts and calibrations throughout the mission trajectory: the first one post-launch (labeled "OPM 1.1" in Fig. 13 (a)), the second one before the Jupiter flyby ("OPM 1.2"), the third shortly after the flyby ("OPM 1.3"), and the final one preceding the separation of the orbiter capsule ("OPM 1.4"). These checkouts are conducted to assess the instrument's condition and monitor potential degradation of sensor elements during the mission, with the expectation that the most significant deterioration may occur during the Jupiter gravity assist maneuver. This assessment involves measuring the dark currents of various sensors as their values increase with displacement damage (performed in previous instruments Jimenez et al. 2012; Arruego et al. 2017; Apestigue et al. 2022), measure the temperatures of the sensors during all the scientific operation due its relationship with dark current values, along with monitoring leakage currents from ASICs' operational amplifiers, which could subsequently affect absolute channel measurements. Utilizing this information helps mitigate radiation-induced effects on channel signals. Additionally, the lamp will be employed for in-situ calibrations. This lamp will produce light that will reflect off reflectors strategically placed inside the aeroshell (following the approach used in previous missions, as described by Ragent et al. 1992). The light will be detected by different channels, facilitating validation of the various sensor chains. Despite being designed to minimize data usage and power consumption, this mode is not considered critical in this regard since it is utilized while the probe is still attached to the orbiter, and these data fall outside the total data budget allocated for the descent probe.

OPM 2: This operational mode serves as a minimal calibration step just before the aeroshell is discarded. At this point, the probe has already begun its descent through the planet's atmosphere (labelled as "OPM 2" in Fig. 13 (b)), and the objective is to acquire the ultimate offset values for each channel, which will serve as references during the descent phase. Consequently, all UMR channels must be measured under dark conditions during OPM 2.

OPM 3: The third operational mode begins when the probe's onboard computer triggers the UMR, signifying the successful deployment of the second parachute (0.1 bar; +55 km height). Then the UMR-OH is exposed to Uranus' atmosphere and initiates the scientific phase (identified as "OPM 3" in Fig. 13 (b)) that will be manage by a sequence timer. During this phase, spanning from this point until crossing the cloud belt at 1-2 bars, precise knowledge of the relative position of the Sun becomes critical for achieving specific scientific objectives. The probe uses a swivel mechanism to decouple its spin from the parachute's and is also equipped with 3 spin vanes to control the rotational rate. The experience of Galileo, described in Lanzerotti et al. 1998, is that the initial spin rate was around 40-35 rpm and was modulated by the aerodynamical system down to 15 rpm during the descent. This implies that at the beginning of the UMR mission, the probe could rotate more than 180° per second and consequently, the sun sensor channels should be sampled at a high rate to be able to capture enough scattering angles. Depending on the characteristics of the inertial sensors integrated into the probe, a subsequent study will be conducted to fine-tune the minimum sampling rate for these channels, ensuring the capability to reconstruct the probe's attitude by combining data from both sensors, but for this first definition, we have considered 5 Hz.

The UMR's B.1 set of detectors should also be sampled at the same rate as the sun position to record scattering angles as comprehensively as possible. The B.2 and C sets of channels will also be measured during this phase at a lower rate of 0.2 Hz which corresponds to 500 meters of vertical resolution.

OPM 4: The last mode is dedicated to characterize the clouds and therefore it starts at a depth of approximately 2 bars ($\sim$768 seconds after the beginning of OPM 3 see Table 5). Sets B.2 and C continue to be sampled as the probe descends further (up to 5-6 bar), but at lower sampling rates (0.07 Hz) due to a reduction in the probe's speed. The D photodetector sets will be utilized in conjunction with the IR lamp in a flashing sequence, with each flash lasting 0.5 seconds. This sequence will be repeated approximately every 14 seconds, resulting in a vertical resolution close to 500 meters.

7 Calibration and Validation Activities

7.1 UV-Visible-NIR Channels Calibration (A, B and C Types)

The calibration method for the Si photodiodes will be an adaptation of the previous work done for the calibration of RDS, that is described in Jiménez et al. 2018. It is based on the spectro-radiometric transfer from a standard lamp to a standard detector in well-controlled laboratory conditions (e.g., Wyatt 1978, 1991; Hülsen et al. 2008; Datla et al. 2016).

In this calibration model it is assumed that wavelength (λ), temperature (T) and incidence angle (θ elevation, φ azimuth sensor coordinates) can be considered as independent variables (Wyatt 1978 and 1991) and thus, the photodiode output signal I (A), could be expressed as:

$$I(T, \varphi, \theta, E_{Sun}) = ARF(\theta, \varphi) \cdot TRF(T) \cdot R_{\lambda_1 Sun}^{\lambda_2} \cdot E_{\lambda_1 Sun}^{\lambda_2} + offset(T) \tag{1}$$

where ARF(θ, φ) is the angular response function of the channel; TRF(T) is the temperature response function or channel dependence with the temperature; $R_{\lambda_1 Sun}^{\lambda_2}$ is the mean responsivity for a channel with $\lambda 1 - \lambda 2$ wavelength, if the calibration is performed with a solar simulator with an $E_{\lambda_1 Sun}^{\lambda_2}$ irradiance level.

To calculate equation (1), the following steps will be undertaken during the calibration procedure: (i) Offset calibration, step that involves utilizing a vacuum cryostat in which the

Table 5 Summary of Operational Modes (OPM) of the UMR during the whole mission. For each, information on the different channels used, the sampling frequency, and the data generated is presented

Operational Mode (OPM)	Mode Rationale	Channel Type used*	Sampling sequence duration (s)	Sampling Rate (Hz)	Vertical resolution (m/sample)	Power (W)	Required Energy (Wh)	Generated Data (kbytes)
1	Health Checkouts	Heating	1800	n/a	n/a	4	2**	0.1**
		All in darkness	100	1		0.8	0.022**	2**
		All light ramp	100	1				5**
2	On-board calibration	Heating	1800	n/a	n/a	4	2	0.1
		All in darkness	100	1		0.8	0.022	2
3	Sun position	A	768	5	19	0.9	0.192	45
	UV	B.1		5	19			102
	Aerosols	B.2		0.2	470	0.6	0.128	3
	Net Flux	C		0.2	470			1.5
	Transparent Heaters	All				0.4	0.008	
4	Aerosols	B.2	2291	0.07	470	0.6	0.381	3
	Net Flux	C		0.07	470			1.5
	Clouds	D		0.07	470	1.25***	2.7E-2	3.8
	Transparent Heaters	All				0.4	0.25	
						TOTAL	**3.0**	**161.9**

*Corresponding with Table 1 classification

**Not accounted for final figures due to the mission phase

***20 Hz Flash of 0.5 s duration, at 50% duty cycle (2.5 W maximum)

OH is exposed to darkness and subjected to a full temperature profile range $(100\,\text{K}-170\,\text{K})$; (ii) Temperature response function calibration using the vacuum cryostat with a constant light level exposure through a sun simulator, covering the complete temperature profile range $(100\,\text{K} - 170\,\text{K})$; (iii) average responsivity calibration, using different steps of light levels of the sun simulator at constant temperatures (it should be repeated for different temperatures); (iv) angular response function calibration, using a collimated and constant level light and a gimbal robotic structure to map the angular response of each channel.

7.2 Mid-IR Channels Calibration (D Type)

The basic equation relating detector output current I_{out} to the external radiation flux is essentially (1). This equation is the results of adapting equations in (Sebastian et al. 2020) (Sebastian et al. 2021) for a photodetector:

$$I_{out} = S\left(T_d\right) \cdot A_s \cdot F_{d-t} \cdot L_t + i_{Sd} \tag{2}$$

where $S\left(T_d\right)$ is the detector responsivity including dependence on temperature, T_d is detector temperature, A_s is the detector area, F_{d-t} is the view factor between the detector and the target (considering in their calculus detector relative angular response), L_t is the irradiance form the target. Consider a flat radiation field, as an extended area blackbody, then L_t is given by the Planck radiance function $B_\lambda(T)$ and can be expressed as:

$$L_t = \int_0^\infty s_{\lambda e} \cdot B_\lambda(T_t)d\lambda \tag{3}$$

where $s_{\lambda e}$ is the detector relative spectral response at wavelength λ and T_t is the target temperature.

The term i_{Sd} is the photodetector current generated by background light, and it accounts for the flux exchange with the inner surfaces of detector package and the external mechanical assemblies conforming the external FoV. Since there is no filter limiting the bandpass of the inner fluxes, they represent an important source of uncertainty (Sebastián et al. 2011; Foote 1999). During operations and descent in Uranus, these fluxes will take a non-zero value because of the thermally challenging environment and their effect will be compensated using the electronics chopping of the IR lamp.

To compute detector output according to the above equation (1), the following set of calibration tests will be performed: (i) Relative angular response. It will use a blackbody source operating above 500 K, a mechanical chopper to modulate blackbody signal, and a pan-and-tilt system as an angular scanning system. (ii) Relative spectral response. It will be performed using a 1000 K SiC global lamp, a monochromator to select wavelengths, and a reference detector to measure the monochromator output for comparison with detector output. (iii) Relative response versus temperature for each channel. The optical head will be mounted on a thermoelectric cooler within a sealed chamber to recreate thermal-vacuum conditions in which the instrument's operating temperatures will be swept. The detector will be exposed to an extended area of blackbody as the radiation source. For each detector operating temperature, two or more blackbody temperatures will be programmed. In this way, a differential process to avoid uncertainties due to background light is implemented (Sebastian et al. 2020). (iv) Absolute responsivity measurements. To implement this calibration, test a blackbody source that fills uniformly the detector's field of view will be used. The use of an extended area or cavity blackbody will be studied, taking into account parameters such as FoV, uniformity of the radiating surface and apparent emissivity. Once again, differential

measurements with different radiation temperatures will be used to mitigate the effects of background light. This calibration approach is based on the heritage of previous space radiometers and pyrometers on board NASA rovers exploring Mars, that have been developed at the Centro de Astrobiología (CSIC-INTA) (Sebastián et al. 2010; Rodriguez-Manfredi et al. 2021).

8 Conclusions

This work describes the concept and design of the Uranus Multi-experiment Radiometer (UMR), a potential instrument for a future probe mission to the Ice Giants. The instrument is dedicated to studying the properties of the hazes and clouds as well as directly estimating the thermal heating rates of Uranus' atmosphere and ultra-violet (UV) radiation levels.

The instrument concept and design has been developed from the heritage of previous radiometers developed at INTA that are or were part of different Martian missions (e.g., ExoMars 2016-2020 or Mars 2020). The strength of the UMR concept lies on its low power consumption, its capacity to operate and survive in extreme environments with cryogenic temperatures, and its lightweight design, making it easy to integrate into probe missions with stringent requirements. Additionally, the instrument unit's arrangement is flexible, making it simple to change to accommodate any future requirements. All of these steps were carried out while also taking into account the high instrument's scientific return.

Declarations

Competing Interests The authors have no conflict of interest to declare that are relevant to the content of this article.

References

Alvarez-Herrero A, Uribe-Patarroyo N, García Parejo P et al (2011) Imaging polarimeters based on liquid crystal variable retarders: an emergent technology for space instrumentation. In: Proc. SPIE 8160, polarization science and remote sensing V, vol 81600Y. https://doi.org/10.1117/12.892732

Alvarez-Herrero A, García Parejo P, Laguna H, Villanueva J, Barandiarán J, Bastide L, Reina M, Royo M (2017) The polarization modulators based on liquid crystal variable retarders for the PHI and METIS instruments for the solar orbiter mission. In: Proc. SPIE 10563, International Conference on Space Optics — ICSO 2014, p 105632Z. https://doi.org/10.1117/12.2304224

Alvarez-Ríos FJ, Jiménez JJ (2017) FOV mask optimization for miniaturized radiometers. In: Proc. SPIE 10562, International Conference on Space Optics — ICSO 2016, 105625A, vol 25. https://doi.org/10.1117/12.2296140

Antonucci E et al (2020) Metis: the Solar Orbiter visible light and ultraviolet coronal imager. Astron Astrophys 642:A10. https://doi.org/10.1051/0004-6361/201935338

Apestigue V, Gonzalo A, Jiménez JJ, Boland J, Lemmon M, de Mingo JR, García-Menendez E, Rivas J, Azcue J, Bastide L et al (2022) Radiation and dust sensor for Mars environmental dynamic analyzer onboard M2020 rover. Sensors 22(8):2907. https://doi.org/10.3390/s22082907

Arridge CS, Agnor CB, André N, Baines KH, Fletcher LN, Gautier D et al (2012) Uranus Pathfinder: exploring the origins and evolution of Ice Giant planets. Exp Astron 33:753. https://doi.org/10.1007/s10686-011-9251-4

Arruego I et al (2016) Sun Irradiance and Dust Sensor Investigations on board the ExoMars 2018 Lander. In: 13th international planetary probe workshop (IPPW-13), Washington DC, Maryland, USA

Arruego I, Apéstigue V, Jiménez-Martín JJ, Martínez-Oter J, Álvarez-Ríos FJ, González-Guerrero M, Rivas J, Azcue J, Martín I, Toledo D et al (2017) DREAMS-SIS: the Solar Irradiance Sensor on-board the ExoMars 2016 lander. Adv Space Res 60:103–120. https://doi.org/10.1016/j.asr.2017.04.002

Aslam S, Achterberg RK, Calcutt SB et al (2020) Advanced net flux radiometer for the ice giants. Space Sci Rev 216:11. https://doi.org/10.1007/s11214-019-0630-x

Atreya SK, Hofstadter MH, In JH et al (2020) Deep atmosphere composition, structure, origin, and exploration, with particular focus on critical in situ science at the Icy Giants. Space Sci Rev 216:18. https://doi.org/10.1007/s11214-020-0640-8

Avduevsky VS, Marov MY, Moshkin BE, Ekonomov AP (1973) Venera 8: measurements of solar illumination through the atmosphere of Venus 1. J Atmos Sci 30:1215–1218. https://doi.org/10.1175/1520-0469(1973)030<1215:VMOSIT>2.0.CO;2

Bayon FS et al (2019) Cdf study report: Ice Giants, ESA. https://sci.esa.int/s/8JgpdVA

Bienstock B (2008) Instrument Accommodation on the Pioneer Venus and Galileo Probes. Sixth International Planetary Probe Workshop (IPPW-6), Atlanta, Georgia, June 21-27, 2008

Boese RW, Twarowski RJ, Gilland J, Hassig RE, Brown FG (1980) The infrared radiometer on the sounder probe of the pioneer Venus mission. IEEE Trans Geosci Remote Sens GE–18(1):97–100. https://doi.org/10.1109/TGRS.1980.350289

Borucki WJ et al (2011) Characteristics of planetary candidates observed by Kepler, II: analysis of the first four months of data. Astrophys J 736:19. https://doi.org/10.1088/0004-637X/736/1/19

Camin DV, Grassi V (2006) Cryogenic behavior of optoelectronic devices for the transmission of analog signals via fiber optics. IEEE Trans Nucl Sci 53(6):3929–3933. https://doi.org/10.1109/TNS.2006.886050

Carlson BE, Rossow WB, Orton GS (1988) Cloud microphysics of the giant planets. J Atmos Sci 45:2066–2081. https://doi.org/10.1175/1520-0469(1988)045<2066:CMOTGP>2.0.CO;2

Datla R, Shao X, Cao C, Wu X (2016) Comparison of the calibration algorithms and SI traceability of MODIS, VIIRS, GOES, and GOES-R ABI sensors. Remote Sens 8(2):126

De Boom CW, Leijtens JAP, van der Heiden N (2006) Micro digital sun sensor: a matchbox miracle. In: 6th international ESA conference on guidance, navigation and control systems. SP-606

Esposito F, Debei S, Bettanini C et al (2018) The DREAMS experiment onboard the schiaparelli module of the ExoMars 2016 mission: design, performances and expected results. Space Sci Rev 214:103. https://doi.org/10.1007/s11214-018-0535-0

Ferri F, Colombatti G, Aboudan A et al (2020) The atmospheric structure of the Ice Giant planets from in situ measurements by entry probes. Space Sci Rev 216:118. https://doi.org/10.1007/s11214-020-00749-9

Foote MC (1999) Temperature stabilization requirements for unchopped thermal detectors. In: Proceedings of SPIE conference on infrared technology and applications XXV, vol 3698

Fulton BJ, Petigura EA, Howard AW, Isaacson H, Marcy GW, Cargile PA, Hirsch LA (2017) The California-Kepler survey. III. A gap in the radius distribution of small planets. Astron J 154(3):109. https://doi.org/10.3847/1538-3881/aa80eb

Genty F, Margueron S, Ould Saad Mamady S, Petit JC, Srour H, Karsaklian dal Bosco A, Sadok J, Huguenin J, Bourig M, Jacquet J (2011) Low Temperature Transparent ITO-based Contacts for Mid-IR Applications. MRS Online Proceedings Library 1327,802. https://doi.org/10.1557/opl.2011.1123

Glebov BL, Waczynski A, Jepsen KS, Miko LR (2018) Stability of device responsivity in silicon photodiodes under cryogenic conditions. Rev Sci Instrum 89(11):113106. https://doi.org/10.1063/1.5053984

Harri A-M, Pichkadze K, Zeleny L, Vazquez L, Schmidt W, Alexashkin S, Korablev O, Guerrero H, Heilimo J, Uspensky M, Finchenko V, Linkin V, Arruego I, Genzer M, Lipatov A, Polkko J, Paton M, Savijärvi H, Haukka H, Siili T, Khovanskov V, Ostesko B, Poroshin A, Diaz-Michelena M, Siikonen T, Palin M, Vorontsov V, Polyakov A, Valero F, Kemppinen O, Leinonen J, Romero P (2017) The MetNet vehicle: a lander to deploy environmental stations for local and global investigations of Mars. Geosci Instrum Method Data Syst 6:103–124. https://doi.org/10.5194/gi-6-103-2017

Hofstadter M, Simon A, Reh K, Elliott J et al (2017) Ice Giants Pre-Decadal Survey Mission Study Report. JPL D-100520. National Aeronautics and Space Administration

Hofstadter M et al (2019) Uranus and Neptune missions: a study in advance of the next planetary science decadal survey. Planet Space Sci 177:104680. https://doi.org/10.1016/j.pss.2019.06.004

Howett CJA, Carlson RW, Irwin PGJ, Calcutt SB (2007) Optical constants of ammonium hydrosulfide ice and ammonia ice. J Opt Soc Am B 24:126–136. https://opg.optica.org/josab/abstract.cfm?URI=josab-24-1-126

Hubbard WB, The Ice Giants Decadal Study Team (2010) Ice Giants Decadal Study. Accessible on the website of the National Academies at http://sites.nationalacademies.org/SSB/SSB_059331

Hülsen G, Gröbner J, Bais A, Blumthaler M, Disterhoft P, Johnsen B, Lantz KO, Meleti C, Schreder J, Vilaplana Guerrero JM et al (2008) Intercomparison of erythemal broadband radiometers calibrated by seven UV calibration facilities in Europe and the USA. Atmos Chem Phys 8(16):4865–4875

Irwin P, Teanby N, de Kok R, Fletcher L, Howett C, Tsang C, Wilson C, Calcutt S, Nixon C, Parrish P (2008) The NEMESIS planetary atmosphere radiative transfer and retrieval tool. J Quant Spectrosc Radiat Transf 109(6):1136–1150. https://doi.org/10.1016/j.jqsrt.2007.11.006

Irwin PGJ, Toledo D, Garland R, Teanby NA, Fletcher LN, Orton GS, Bézard B (2018) Detection of hydrogen sulfide above the clouds in Uranus's atmosphere. Nat Astron 2:420–427. https://doi.org/10.1038/s41550-018-0432-1

Irwin PGJ, Teanby NA, Fletcher LN, Toledo D, Orton GS, Wong MH et al (2022) Hazy blue worlds: a holistic aerosol model for Uranus and Neptune, including dark spots. J Geophys Res, Planets 127:e2022JE007189. https://doi.org/10.1029/2022JE007189

Irwin PGJ, Dobinson J, James A et al (2023) Spectral determination of the color and vertical structure of dark spots in Neptune's atmosphere. Nat Astron. https://doi.org/10.1038/s41550-023-02047-0

Jimenez JJ et al (2012) Proton Monitor Las Dos Torres: First Intercomparison of In-Orbit Results. IEEE Trans Nucl Sci 59(4):1092–1098. https://doi.org/10.1109/TNS.2012.2198241

Jiménez JJ, Álvarez JF, Gonzalez-Guerrero M, Apéstigue V, Martín I, Fernández JM, Fernán AA, Arruego I (2018) Calibration OGSEs for multichannel radiometers for Mars atmosphere studies. CEAS Space J 10:127. https://doi.org/10.1007/s12567-018-0194-8

Karkoschka E (2001) Uranus's apparent seasonal variability in 25 HST filters. Icarus 151(1):84–92. https://doi.org/10.1006/icar.2001.6599

Knollenberg RG, Gilland JR (1980) Pioneer Venus sounder probe particle size spectrometer. IEEE Trans Geosci Remote Sens GE–18(1):100–104. https://doi.org/10.1109/TGRS.1980.350290

Lanzerotti LJ, Rinnert K, Carlock D, Sobeck CK, Dehmel G (1998) Spin rate of Galileo probe during descent into the atmosphere of Jupiter. J Spacecr Rockets 35(1):100–102. https://doi.org/10.2514/3.27003

Mandt KE, Mousis O, Marty B et al (2015) Constraints from comets on the formation and volatile acquisition of the planets and satellites. Space Sci Rev 197:297–342. https://doi.org/10.1007/s11214-015-0161-z

Marov MY, Lystesev VE, Lebedev VN, Lukashevich NL, Shari VP (1980) The structure and microphysical properties of the Venus clouds: Venera 9, 10, and 11 data. Icarus 44(3):608–639. https://doi.org/10.1016/0019-1035(80)90131-1

Martin-Ortega A, Arruego I, Traseira I, Andres N et al (2017) MicroMED processing unit: enhanced computing for planetary exploration payloads. In: ExoMars atmospheric science and missions workshop, 26–30 March 2017 Saariselkä, Finland

Morath CP, Garduno EA, Jenkins GD, Steenbergen EA, Cowan VM (2019) Effects of 63 MeV proton-irradiation on the dark-current in III-V-based, unipolar barrier infrared detectors. Infrared Phys Technol 97:448–455. https://doi.org/10.1016/j.infrared.2018.12.033

Moses JI, Fletcher LN, Greathouse TK, Orton GS, Seasonal HV (2018) Stratospheric photochemistry on Uranus and Neptune. Icarus 307:124–145. https://doi.org/10.1016/j.icarus.2018.02.004

Mousis O, Atkinson DH, Cavalié T, Fletcher LN, Amato MJ, Aslam S et al (2018) Scientific rationale for Uranus and Neptune in situ explorations. Planet Space Sci 155:12. https://doi.org/10.1016/j.pss.2017.10.005

Mousis O, Atkinson DH, Ambrosi R et al (2022) In situ exploration of the giant planets. Exp Astron 54:975–1013. https://doi.org/10.1007/s10686-021-09775-z

Nagakubo A, Ogi H, Hirao M (2015) Refractive index and extinction coefficient of Si at 400 nm between 10 and 300K. Jpn J Appl Phys 54(12):128001. https://doi.org/10.7567/JJAP.54.128001

National Academies of Sciences, Engineering, and Medicine (2022) Origins, worlds, and life: a decadal strategy for planetary science and astrobiology 2023-2032. The National Academies Press, Washington. https://doi.org/10.17226/26522

Ragent B, Wong T, Blamont JE, Eskovitz AJ, Harnett LN, Pallai A (1980) Sounder and small probe nephelometer experiment. IEEE Trans Geosci Remote Sens GE–18:111–117. https://doi.org/10.1109/TGRS.1980.350292

Ragent B, Privette CA, Avrin P et al (1992) Galileo probe nephelometer experiment. Space Sci Rev 60:179–201. https://doi.org/10.1007/BF00216854

Ramos J et al (2013) SEE characterization of the AMS 0.35 µm CMOS technology. In: Proceedings of the conference on radiation effects on components and systems (RADECS 2013)

Ramos-Martos J et al (2012) Evaluation of the AMS 0.35 um CMOS technology for use in space applications. In: Proceedings of the Analog and Mixed-Signal Integrated Circuits for Space Applications (AMICSA 2012)

Renard JB, Mousis O, Rannou P et al (2020) Counting and phase function measurements with the LON-SCAPE instrument to determine physical properties of aerosols in Ice Giant planet atmospheres. Space Sci Rev 216:28. https://doi.org/10.1007/s11214-020-00653-2

Rodriguez-Manfredi JA, de la Torre Juárez M, Alonso A et al (2021) The Mars environmental dynamics analyzer, MEDA. A suite of environmental sensors for the Mars 2020 mission. Space Sci Rev 217:48. https://doi.org/10.1007/s11214-021-00816-9

Sahu K, Leidecker H, Lakins D (2003) EEE-INST-002: Instructions for EEE PartsSelection, Screening, Qualification, and Derating. NASA/TP-2003-212242

Schmitt B, Bollard P, Albert D, Bonal L (2012) SSHADE/GhoSST: 'Grenoble astropHysics and planetOlogy Solid Spectroscopy and Thermodynamics' database. SSHADE (OSUG Data Center). Service/Database. https://doi.org/10.26302/SSHADE/GHOSST

Sebastián E, Armiens C, Gómez-Elvira J, Zorzano MP, Martinez-Frias J, Esteban B, Ramos M (2010) The rover environmental monitoring station ground temperature sensor: a pyrometer for measuring ground temperature on Mars. Sensors 10(10):9211–9231. https://doi.org/10.3390/s101009211

Sebastián E, Armiens C, Gómez-Elvira J (2011) Infrared temperature measurement uncertainty for unchopped thermopile in presence of case thermal gradients. Infrared Phys Technol 54:75–83. https://doi.org/10.1016/j.infrared.2010.12.038

Sebastian E, Martínez GM, Ramos M, Haenschke F, Ferrándiz R, Fernández M, Rodriguez Manfredi JA (2020) Radiometric and angular calibration tests for the MEDA-TIRS radiometer onboard NASA's Mars 2020 mission. Measurement 164:107968. https://doi.org/10.1016/j.measurement.2020.107968

Sebastian E et al (2021) Thermal calibration of the MEDA-TIRS radiometer onboard NASA's perseverance rover. Acta Astronaut 182:144–159

Simon A, Nimmo F, Anderson RC (2021) Journey to an Ice Giant System. Uranus Orbiter & Probe. Planetary Mission Concept Study for the 2023-2032 Decadal Survey. National Aeronautics and Space Administration

Solanki SK et al (2020) The polarimetric and helioseismic imager on solar orbiter. Astron Astrophys 642:A11. https://doi.org/10.1051/0004-6361/201935325

Sordo-Ibañez S et al (2014) A rad-hard multichannel front-end readout ASIC for space applications. In: 2014 IEEE Metrology for Aerospace (MetroAeroSpace), Benevento, Italy, pp 180–184. https://doi.org/10.1109/MetroAeroSpace.2014.6865916

Sromovsky LA, Revercomb HE, Suomi VE (1980) Pioneer Venus small probes net flux radiometer experiment. IEEE Trans Geosci Remote Sens GE–18(1):117–122. https://doi.org/10.1109/TGRS.1980.350293

Sromovsky LA, Best FA, Revercomb HE et al (1992) Galileo Net Flux Radiometer experiment. Space Sci Rev 60:233–262. https://doi.org/10.1007/BF00216856

Steenbergen EH, Massengale JA, Cowan VM, Lin Z, Zhang Y-H, Morath CP (2013) Proton radiation effects on the photoluminescence of infrared InAs/InAsSb superlattices. In: Proc. SPIE 8876, nanophotonics and macrophotonics for space environments VII, p 887609. https://doi.org/10.1117/12.202687

Sun Q, Gutiérrez JLR, Deep YX (2023) Neural network-based 4-quadrant analog sun sensor calibration. Space Sci Technol 3:0024. https://doi.org/10.34133/space

Toledo D, Arruego I, Apéstigue V, Jiménez JJ, Gómez L, Yela M, Rannou P, Pommereau J-P (2017) Measurement of dust optical depth using the solar irradiance sensor (SIS) onboard the ExoMars 2016 EDM. Planet Space Sci 138:33–43. https://doi.org/10.1016/j.pss.2017.01.015

Toledo D, Gómez L, Apéstigue V, Arruego I, Smith M, Munguira A et al (2023) Twilight mesospheric clouds in Jezero as observed by MEDA Radiation and Dust Sensor (RDS). J Geophys Res, Planets 128:e2023JE007785. https://doi.org/10.1029/2023JE007785

Tomasko MG et al (1980) Pioneer Venus sounder probe solar flux radiometer. IEEE Trans Geosci Remote Sens GE–18(1):93–97. https://doi.org/10.1109/TGRS.1980.350288

Tomasko M, Buchhauser D, Bushroe M et al (2002) The descent imager/spectral radiometer (DISR) experiment on the Huygens entry probe of Titan. Space Sci Rev 104:469–551. https://doi.org/10.1023/A:1023632422098

Vázquez D, Ceballos J, Espejo S (2018) SIS20: a CMOS ASIC for solar irradiance sensors in Mars surface. In: AMICSA 2018, Leuven, Begium

Wyatt CL (1978) Radiometric calibration: theory and methods. Academic Press, New York

Wyatt CL (1991) Electro-optical system design for information processing. McGraw-Hill, New York

Zelenyi LM, Korablev OI, Rodionov DS et al (2015) Scientific objectives of the scientific equipment of the landing platform of the ExoMars-2018 mission. Sol Syst Res 49:509–517. https://doi.org/10.1134/S0038094615070229

Authors and Affiliations

V. Apéstigue[1] [ID] **· D. Toledo[1] · P.G.J. Irwin[2] · P. Rannou[3] · A. Gonzalo[1] ·
J. Martínez-Oter[1] · J. Ceballos-Cáceres[4] · J. Azcue[1] · J.J. Jiménez[1] · E. Sebastian[1,5] ·
M. Yela[1] · M. Sorribas[1] · J.R. de Mingo[1] · A. Martín-Ortega[1] · T. Belenger[1] · M. Alvarez[1] ·
D. Vázquez-García de la Vega[4] · S. Espejo[4] · I. Arruego[1]**

✉ V. Apéstigue
   apestiguepv@inta.es

1   Instituto Nacional de Técnica Aeroespacial (INTA), Ctra. Aljalvir Km 4, Torrejón de Ardoz, 28850, Madrid, Spain

2   Department of Physics, University of Oxford, Parks Rd, Oxford, OX1 3PU, UK

3   Université de Reims Champagne-Ardenne, Reims, France

4   Instituto de Microelectrónica de Sevilla, Sevilla, Spain

5   Centro de Astrobiología (INTA-CSIC), Madrid, Spain